



## In situ assembly of graphene sheets-supported SnS<sub>2</sub> nanoplates into 3D macroporous aerogels for high-performance lithium ion batteries

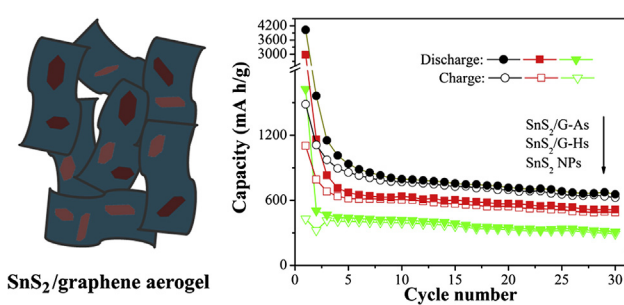
Xin Jiang, Xiaoling Yang, Yihua Zhu\*, Jianhua Shen, Kaicai Fan, Chunzhong Li

*Key Laboratory for Ultrafine Materials of Ministry of Education, School of Materials Science and Engineering, East China University of Science and Technology, 130 Meilong Road, Shanghai 200237, China*

### HIGHLIGHTS

- 3D aerogels consisted of graphene-supported SnS<sub>2</sub> nanoplates are prepared by hydrothermal assembly and freeze-drying process.
- As-prepared aerogels show interconnected networks, large surface area and large numbers of macropores.
- As-prepared aerogels exhibit high-rate capability and cycling stability when used as an anode.

### GRAPHICAL ABSTRACT



### ARTICLE INFO

#### Article history:

Received 8 November 2012

Received in revised form

4 March 2013

Accepted 12 March 2013

Available online 21 March 2013

#### Keywords:

Graphene

Tin disulfide

Anode

Lithium ion batteries

Aerogels

### ABSTRACT

Three-dimensional (3D) SnS<sub>2</sub>/graphene aerogels (SnS<sub>2</sub>/G-As) have been successfully fabricated via an in situ macroscopy self-assembly of graphene sheets which embedded SnS<sub>2</sub> nanoplates in a hydrothermal process, and then freeze-drying to maintain the 3D monolithic architectures. The graphene sheets in high concentration will be easily restacked into 3D architectures driven by combined hydrophobic and π–π stacking interactions during hydrothermal reduction process, meanwhile SnS<sub>2</sub> facilitate stabilizing such novel graphene networks. The obtained SnS<sub>2</sub>/G-As show interconnected graphene networks, large surface area and large numbers of macropores. The novel 3D architectures in SnS<sub>2</sub>/G-As, which can provide rich sites for absorbing lithium ions and facilitate electrolyte contact as well as ionic diffusion, combined with the synergistic effect between the layered SnS<sub>2</sub> and the graphene make SnS<sub>2</sub>/G-As achieve high reversible capacity (656 mA h g<sup>-1</sup> with a coulombic efficiency of over 95% after 30 cycles) and excellent rate capability (240 mA h g<sup>-1</sup> at the rate of 1000 mA g<sup>-1</sup>) when used as an anode in rechargeable LIBs.

© 2013 Elsevier B.V. All rights reserved.

### 1. Introduction

Lithium ion batteries (LIBs) is the main power sources for portable electronic devices and electrical/hybrid vehicles owing to their high energy density, light weight, and long service life [1,2]. Electrode materials wherein are a determining factor for the battery performance. The conventional graphite anodes have suffered

a relatively low Li storage capacity of 372 mA h g<sup>-1</sup>. Thus, it's necessary to find alternative anode materials with high capacity to meet the ever-growing performance demands [3–5]. To date, some metal sulfides such as MoS<sub>2</sub>, WS<sub>2</sub> and SnS<sub>2</sub> have been actively pursued due to their higher theoretical capacities [6–8]. As a typical transition metal sulfide, SnS<sub>2</sub> possesses a high theoretical specific capacity of 645 mA h g<sup>-1</sup> and superior physicochemical properties due to the layered hexagonal graphite-like type structure, which is composed of tin atoms sandwiched between two layers of hexagonally close packed sulfur atoms. The special layered structure with swelling tolerant hosting spaces can facilitate the

\* Corresponding author. Tel.: +86 21 64252022; fax: +86 21 64250624.

E-mail address: [yhzhu@ecust.edu.cn](mailto:yhzhu@ecust.edu.cn) (Y. Zhu).

moving of  $\text{Li}^+$  ions and electrons through the active materials and compensate the alloying/dealloying volume change to some degree, thus making the higher capacity and improved cycling stability possible [7]. However, the still unavoidable large volume changes and loss of electrical contact during electrochemical cycles can result in sharp decrease in capacity of  $\text{SnS}_2$  [9,10]. One method of lessening the volume expansion in tin-based electrodes is to prepare various  $\text{SnS}_2$  nanostructures with different morphologies, such as nanoflakes, nanospheres and nanoflowers [11–15].

Other researches focus on combining  $\text{SnS}_2$  with carbonaceous materials [16,17]. Graphene, a monolayer of carbon atoms with a tight packing of honeycomb lattice, has attracted considerable research interest for many applications because of its unique structure and special properties [18–20]. Its high theoretical surface area, exceptional electrical and mechanical properties, and chemical stability enable graphene and graphene-based composites as high-capacity anode materials with large initial discharge capacity and reversible capacity [21–28]. As an ideal matrix, graphene nanosheets can act as both a conductive channel to enhance electron transport and electrical contact with electrochemically active materials, and a “buffer zone” to cushion the internal stress induced by the volume expansion/shrinkage of these electrochemically active phases during  $\text{Li}^+$  insertion/extraction process. Luo et al. have reported a facile approach to fabricate 2D graphene– $\text{SnS}_2$  (G– $\text{SnS}_2$ ) hybrids by transforming tin oxide nanoparticles into 2D tin disulfide nanoplates directly on/between graphene nanosheets [17]. The improved electrochemical performances have been achieved for lithium ion batteries using G– $\text{SnS}_2$  as the anode.

However, there are no reports on the direct preparation of 3D architectures of  $\text{SnS}_2$ /graphene as an anode in LIBs. It is believed that integration of individual 2D graphene sheets into macroscopic structures can further realize the full potential of graphene. For this purpose, plenty of self-assembled graphene aerogels (GAs) and composites of 3D graphene embedded metal or metal oxide nanoparticles have been synthesized successfully by diverse methods [29–31]. Graphene-assembled architectures can adjust the hierarchical morphology with high surface-area-to-volume ratios and form macroscopic, large-size monolithic materials, hence offering great technological promise for a variety of sustainable applications, such as energy storage, adsorption, and catalysis [32–34]. In particular, GAs, as a new class of ultralight and porous carbon materials, are associated with 3D interconnected networks and excellent mechanical stability as well as electrical conductivity. When used as electrodes for LIBs, they can provide multidimensional electron transport pathways and minimize transport distances between electrode and electrolyte, thus leading to improved rate performance and cycling stability.

Herein, we report a facile *in situ* hydrothermal method for self-assembly of graphene sheets which embedded  $\text{SnS}_2$  nanoplates, following freeze dry to form 3D  $\text{SnS}_2$ /graphene aerogels ( $\text{SnS}_2/\text{G-As}$ ), as illustrated in Fig. 1. High concentration of graphite oxide (GO) and tin (IV) chloride pentahydrate ( $\text{SnCl}_4 \cdot 5\text{H}_2\text{O}$ ) was selected as starting materials. Due to the many functional groups on the surface of GO, such as carboxyl, hydroxyl and epoxy groups,  $\text{Sn}^{4+}$  homogeneously dispersing in the aqueous suspension tightly adsorbed onto GO surface via the electrostatic interaction [35]. Reduced GO in high concentration would be self-assembled together to form a 3D network architectures during hydrothermal reduction process. While  $\text{H}_2\text{S}$ , which was released from  $\text{NH}_2\text{CSNH}_2$  at high temperature, promoted the formation of  $\text{SnS}_2$  nanoplates. Thus  $\text{SnS}_2$  NPs were simultaneously embedded into the graphene networks and distributed homogeneously on to the both sides of the graphene nanosheets to form a 3D  $\text{SnS}_2$ /graphene hydrogel. After freeze-drying to maintain the 3D monolithic architectures, a light green porous aerogel was finally obtained. Due to the unique

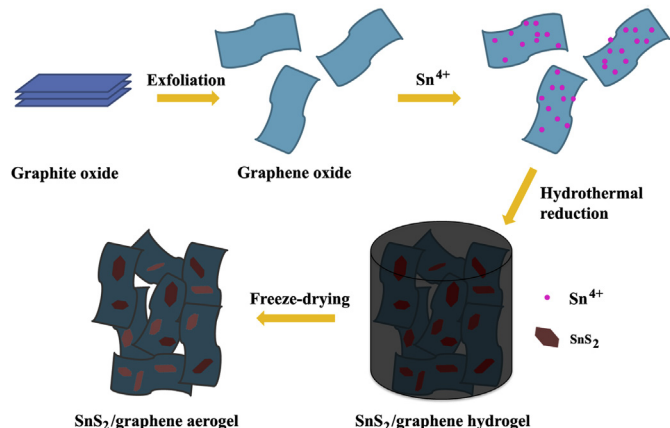


Fig. 1. Fabrication process of 3D  $\text{SnS}_2$ /graphene aerogels ( $\text{SnS}_2/\text{G-As}$ ).

morphology and synergistic effects of the different components, the as-formed aerogel exhibited a high capacity and rate performance as an active Li ion battery electrode. For comparison, pure  $\text{SnS}_2$  NPs and 2D  $\text{SnS}_2$ /graphene hybrids ( $\text{SnS}_2/\text{G-Hs}$ ) were also prepared in similar process but without adding GO or using low concentration of GO as starting materials, respectively.

## 2. Experimental

### 2.1. Chemicals

Graphite powder and Tin (IV) chloride pentahydrate ( $\text{SnCl}_4 \cdot 5\text{H}_2\text{O}$ ) were purchased from Sinopharm Chemical Reagent Co., Ltd. Thiourea ( $\text{NH}_2\text{CSNH}_2$ ) was purchased from Shanghai Lingfeng Chemical Reagent Co. Ltd. All the chemicals were of analytical grade and used as received. Double distilled water was used in all experiments.

### 2.2. Preparation of 3D $\text{SnS}_2$ /graphene aerogels ( $\text{SnS}_2/\text{G-As}$ )

Graphite oxide (GO) was prepared from natural graphite flakes by a modified Hummers method [36].  $\text{SnS}_2/\text{G-As}$  were prepared by a combined hydrothermal assembly and freeze-drying process. In a typical experiment, a 25 mL GO (3 mg mL<sup>-1</sup>) aqueous dispersion was firstly treated by sonication for 1 h, forming a brown dispersion. 1.2 g of Tin (IV) chloride pentahydrate ( $\text{SnCl}_4 \cdot 5\text{H}_2\text{O}$ ) was added to the above solution and the mixed solution was stirred constantly for 30 min. Afterward, 0.8 g of thiourea ( $\text{NH}_2\text{CSNH}_2$ ) was added, followed by stirring for another 30 min. The resulting stable suspension was sealed in a 50 mL Teflon-lined stainless steel autoclave and hydrothermally at 190 °C for 16 h. After the hydrothermal treatment was completed, a hydrogel of reduced GO, which embedded  $\text{SnS}_2$  NPs was obtained. The product was dialyzed with distilled (DI) water for 48 h following freeze-drying, thus forming  $\text{SnS}_2/\text{G-As}$  with 3D networks. For comparison, pure  $\text{SnS}_2$  NPs and 2D  $\text{SnS}_2/\text{G-Hs}$  were also prepared in similar process but without adding GO or using low concentration of GO (1 mg mL<sup>-1</sup>) as starting materials, respectively.

### 2.3. Structure and morphology characterization

The wide-angle (10°–80°, 40 kV/200 mA) powder X-ray diffraction (XRD) measurements were carried out by a polycrystalline X-ray diffractometer (RIGAKU, D/MAX 2550 VB/PC,  $\lambda = 1.5406 \text{ \AA}$ ) under room temperature. Raman spectra were recorded on an inVia Raman microprobe with 514 nm laser excitation. X-ray photoelectron spectroscopy (XPS) was tested on an ESCALab 250Xi X-ray

photoelectron spectrometer with a Mg K $\alpha$  as source and the C1s peak at 284.6 eV as an internal standard. The transmission electron microscopy (TEM) and scanning electron microscopy (SEM) images were obtained using a JEM-2100 microscope operated at 200 kV and a JEOL SM-6360LV microscope equipped with an energy dispersive X-ray analyzer (EDX), respectively. Adsorption–desorption measurements were conducted on a Micromeritics ASAP 2010 apparatus at 77 K using nitrogen as the adsorption gas. Surface area determination and pore volume and size analysis were performed by Brunauer–Emmett–Teller (BET) and Barrett–Joyner–Halenda (BJH) methods. The thermogravimetric (TG) measurement was carried out with a Mettler STARe thermal analyzer in a temperature range of 25–800 °C and in an air atmosphere at the heating rate of 10 °C min<sup>-1</sup>.

#### 2.4. Electrochemical measurements

The electrochemical tests were measured using two-electrode cells assembled in an argon-filled glovebox. Li sheets served as the counter electrode and reference electrode, and a polypropylene film (Celgard 2400) was used as a separator. The electrolyte was a 1.0 M LiPF<sub>6</sub> solution in a mixture 50:50 (w:w) of ethylene carbonate (EC) and diethyl carbonate (DMC). The working electrodes were prepared by a slurry coating procedure. The slurry consisted of 70 wt % active materials, 15 wt % acetylene black, and 15 wt % polyvinylidene fluorides (PVDF) were dissolved in *N*-methyl-2-pyrrolidinone. The slurry was spread on copper foil, which acted as a current collector, and dried at 80 °C for 12 h under vacuum. Galvanostatic charge/discharge cycles were carried out on a LAND-CT2001A battery tester between 0.01 and 3.00 V at various current densities. Cyclic voltammetry (0.01–3.00 V, 0.5 mV s<sup>-1</sup>) was performed using an electrochemical workstation (CHI660D).

### 3. Results and discussion

Fig. 2 showed the photographs of three kinds of samples. Compared with the yellow solution of pure SnS<sub>2</sub> NPs (left in Fig. 2),

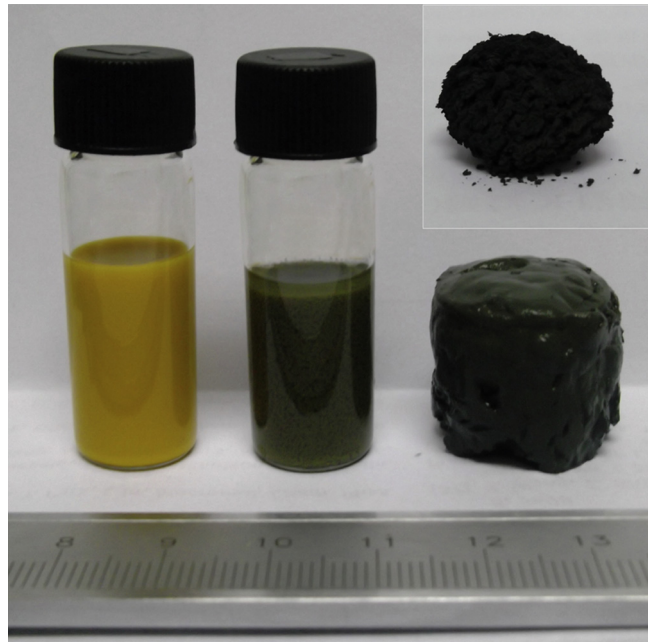


**Fig. 2.** The photographs of three kinds of samples: SnS<sub>2</sub> NPs (left), SnS<sub>2</sub>/G-Hs (middle), the SnS<sub>2</sub>/G-As before freeze-drying process (right), the SnS<sub>2</sub>/G-As after freeze-drying process (Inset).

the color of the obtained SnS<sub>2</sub>/G-Hs turned to green, due to the incorporation of graphene sheets (middle in Fig. 2). The resultant SnS<sub>2</sub>/G hydrogels containing about 94.3 wt % water were about ~15 mm in diameter and ~20 mm in height (right in Fig. 2). It was obvious to see porous structures in the corresponding aerogels after a freeze-drying method to remove the water. Besides, irregular 3D shape was obtained, which was assigned to the partial destroyed of monolithic architectures during the freeze-drying process (Inset in Fig. 2).

Fig. 3a showed the X-ray diffraction (XRD) patterns of three as-prepared samples. The SnS<sub>2</sub> NPs exhibited high crystallinity and a typical hexagonal structure, which was in accordance with those established by JCPDS card number JCPDS 23-0677. The 2D SnS<sub>2</sub>/G-Hs and 3D SnS<sub>2</sub>/G-As composites basically retained the position of diffraction peaks of pure SnS<sub>2</sub> NPs. However, the intensity of all the diffraction peaks of SnS<sub>2</sub> decreased after graphene added, especially the (001) plane peaks at  $2\theta = 15.1^\circ$ , which suggested that the incorporation of the graphene considerably inhibited the (001) plane growth of SnS<sub>2</sub> crystals in the composites. Additionally, no apparent diffraction peak could be identified at 20–30°, indicating that SnS<sub>2</sub> NPs were efficiently deposited on the graphene surface and suppressed the stacking of graphene layers [37,38]. Further insights of the structural and electronic properties of composites were obtained from Raman spectrum (Fig. 3b). A strong Raman

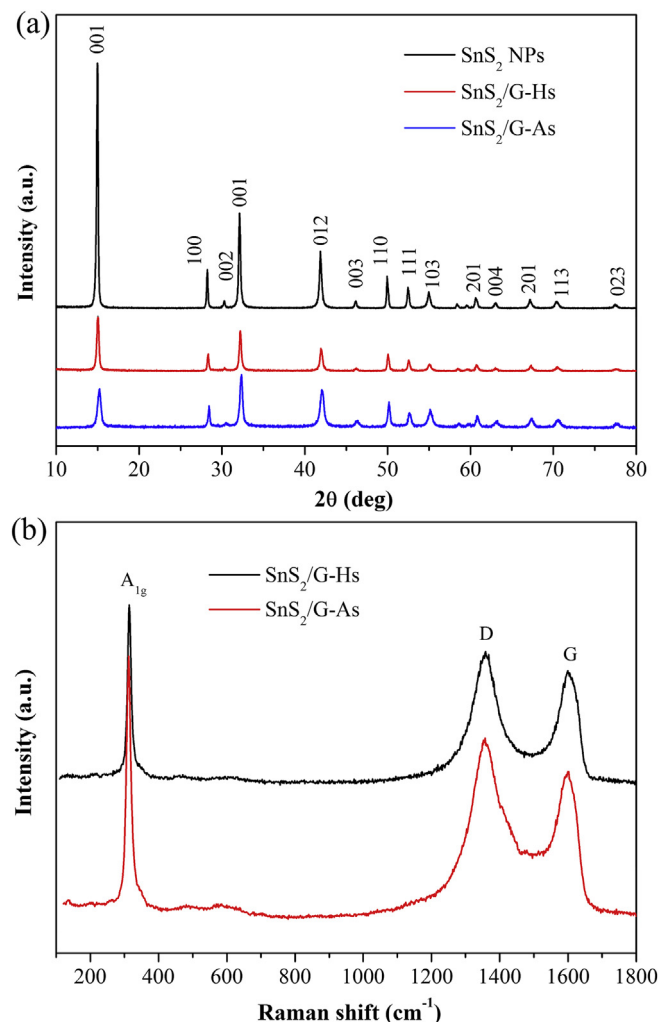


**Fig. 3.** The wide-angle XRD patterns of SnS<sub>2</sub> NPs, SnS<sub>2</sub>/G-Hs and SnS<sub>2</sub>/G-As (a). Raman spectra of SnS<sub>2</sub>/G-Hs and SnS<sub>2</sub>/G-As (b).

peak located at about  $314\text{ cm}^{-1}$  was observed, which could be assigned to the  $A_{1g}$  mode of  $\text{SnS}_2$  according to the group theory analysis given by Lucovsky et al. [39]. A single D-band at  $\sim 1358\text{ cm}^{-1}$  as a breathing mode of k-point phonons of  $A_{1g}$  symmetry, which was attributed to edges, other defects and disordered carbon, and a G-band at  $\sim 1600\text{ cm}^{-1}$  originating from the zone center  $E_{2g}$  mode, which corresponded to ordered  $\text{sp}^2$ -bonded carbon atoms, were observed for both of two composites [40]. The  $I_D/I_G$  intensity ratio can indicate the disorder degree and average size of the  $\text{sp}^2$  domains. Comparing with  $\text{SnS}_2/\text{G-Hs}$ ,  $\text{SnS}_2/\text{G-As}$  displayed an increase D/G intensity ratio, which could be assigned to formation of 3D porous graphene networks upon hydrothermal reduction of high concentration of GO, inducing more defects and disorders [41]. Both XRD and Raman measurements confirmed the successful integration of graphene sheets and  $\text{SnS}_2$  NPs.

The X-ray photoelectron spectroscopy (XPS) measurements were conducted to investigate chemical composition of  $\text{SnS}_2/\text{G-As}$  (Fig. 4). The survey spectrum of  $\text{SnS}_2/\text{G-As}$  showed the distinguished peaks centered about 486.60 eV, 284.60 eV, and 161.60 eV, corresponding to the Sn 3d, C 1s and S 2p, respectively (Fig. 4a). In the C 1s XPS spectrum (Fig. 4b), the main peak at 284.60 eV was related to the graphitic carbon ( $\text{sp}^2$  carbon). The long tail observed at the higher binding energy indicated the presence of trace hydroxyl and epoxy C–O (286.50 eV) and carbonyl C=O (287.80 eV) bonding nature. The reduced content of the components associated with oxygenated functional groups revealed that the GO could be significantly reduced to graphene during the hydrothermal progress. In the high-resolution spectrum for the Sn 3d region (Fig. 4c),  $\text{SnS}_2/\text{G-As}$  presented a predominant Sn 3d<sub>5/2</sub> at 487.05 eV and Sn 3d<sub>3/2</sub> at 495.45 eV, and no peak at 486.30 eV was detected indicating the absence of Sn–C direct bonding, which was in

agreement with the reported data [42]. In addition, the S 2p spectrum showed the presence of S 2p<sub>3/2</sub> at 161.75 eV and S 2p<sub>1/2</sub> at 162.95 eV, which were attributed to the binding energies of  $\text{SnS}_2$  (Fig. 4d) [42,43].

The morphology of the final products was further characterized by SEM and TEM. As shown in Fig. 5a, the pure  $\text{SnS}_2$  displayed a 2D plate-like hexagonal structure with the diameter of about 600 nm, which mainly attributed to its crystal growth habit [44]. When GO was predispersed in hydrothermal solution, a sheet-like graphene could be clearly seen and the hexagonal  $\text{SnS}_2$  nanoplates with the diameter of about 300 nm were homogeneously dispersed on the wrinkling graphene surface (Fig. 5b). Fig. 5(c and d) showed different-magnification SEM images of a cross-section of as-prepared  $\text{SnS}_2/\text{G-As}$ . The flexible graphene sheets were easily self-assembled together by partial overlapping or coalescing as the physical cross-linking sites to form the 3D network architectures during the hydrothermal process [29]. Thus, when the high concentration of GO was selected as starting material, the as-prepared  $\text{SnS}_2/\text{G-As}$  exhibited 3D interconnected networks with macroporous architectures and the pore sizes were in the range of submicrometer to several micrometers (Fig. 5c). The enlarged view of the composite revealed that the pore walls were assembled of the curved layers of graphene sheets with many hexagonal  $\text{SnS}_2$  nanoplates directly grown on them (Fig. 5d), which were similar to those in Fig. 5b. Nitrogen adsorption–desorption analysis revealed a BET surface area of up to  $172.38\text{ m}^2\text{ g}^{-1}$  for  $\text{SnS}_2/\text{G-As}$ . The isotherm curve exhibited a type-IV behavior, indicating the existence of plentiful mesopores and macropores in  $\text{SnS}_2/\text{G-As}$  (Fig. S1a). Based on the BJH method, much of the pore volume ( $0.30\text{ cm}^3\text{ g}^{-1}$ ) lied in the 3.14–100 nm range with a sharp peak at 3.88 nm and a broad one at 31.81 nm (Fig. S1b). The relatively large

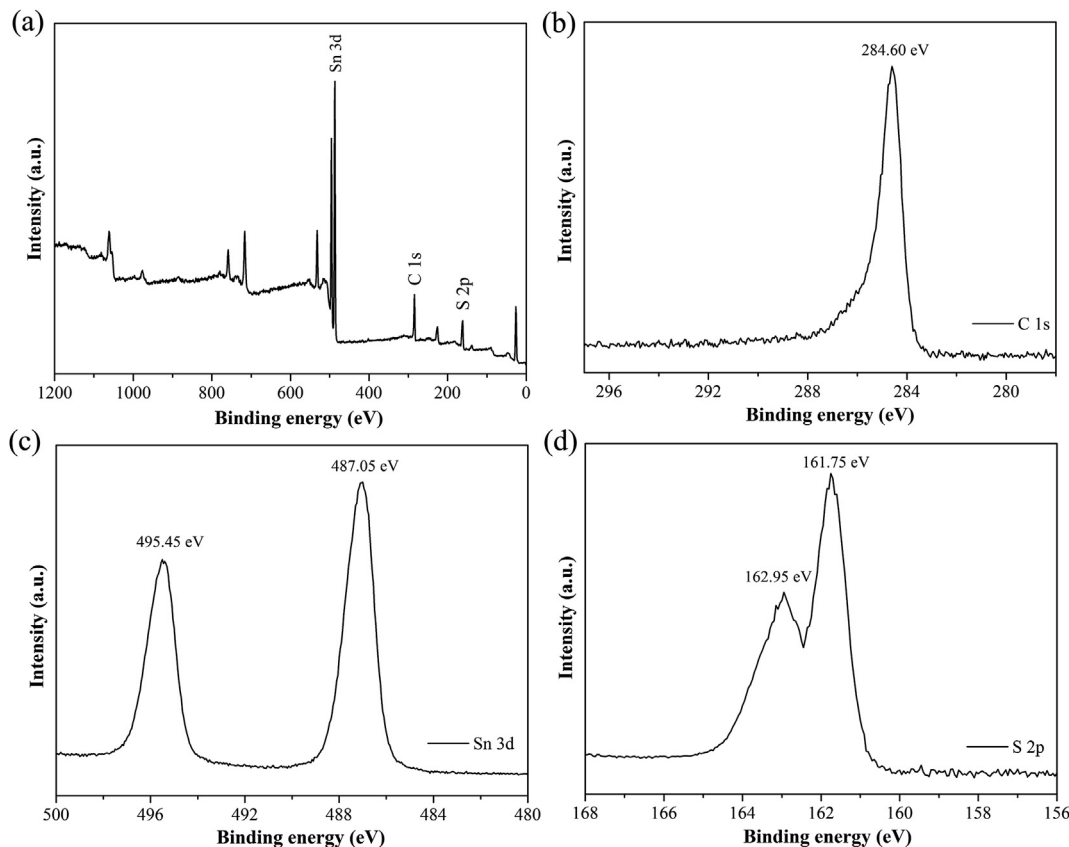


**Fig. 4.** XPS profile of  $\text{SnS}_2/\text{G-As}$ : survey spectra (a), C 1s (b), Sn 3d (c), and S 2p (d) core levels.

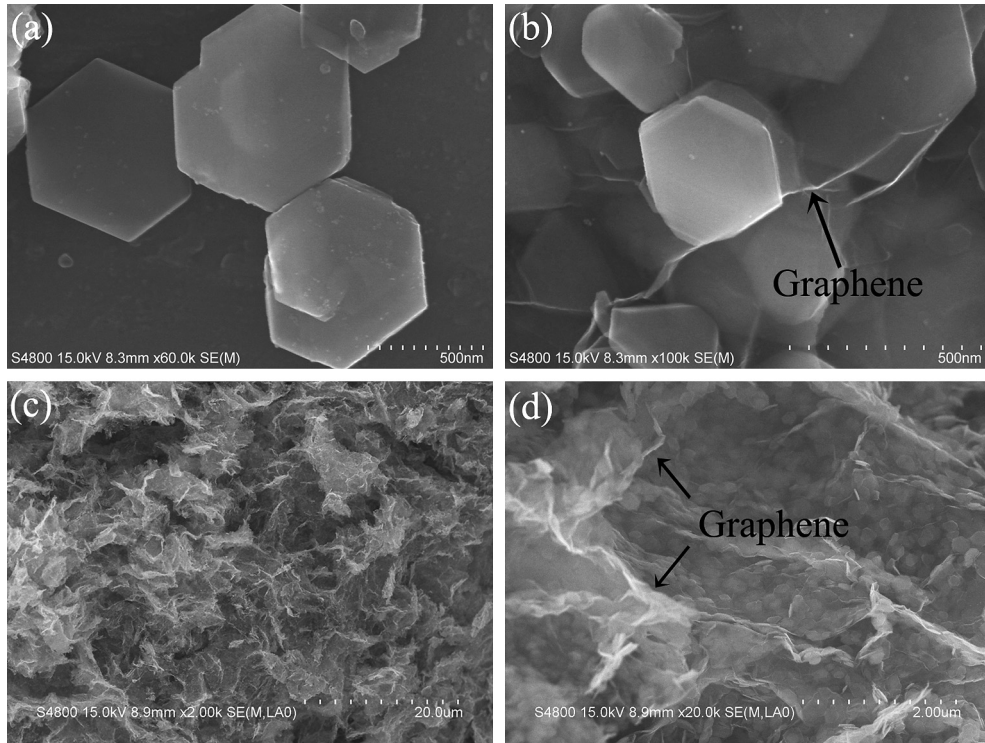


**Fig. 5.** SEM images of the up-side of  $\text{SnS}_2$  NPs (a) and  $\text{SnS}_2/\text{G-Hs}$  (b). Low-magnification (c) and high-magnification (d) SEM images of the cross section of  $\text{SnS}_2/\text{G-As}$ .

specific surface area and a number of hierarchical pores were beneficial for electrolyte access [45].

Fig. 6a presented TEM image of  $\text{SnS}_2/\text{G-As}$ , in which the flexible and ultrathin graphene could be discerned. Moreover, the estimated average diameter of  $\text{SnS}_2$  nanoplates in  $\text{SnS}_2/\text{G-As}$  is about 200 nm, which was quite smaller than that in pure  $\text{SnS}_2$

(600 nm) and  $\text{SnS}_2/\text{G-Hs}$  (300 nm). Notably, three samples were prepared using a similar route with different concentration of GO. GO and reduced GO sheets served as the substrate for the nucleation and growth of  $\text{SnS}_2$  into a layered structure, thus significantly affecting the sizes of the obtained  $\text{SnS}_2$  nanoplates [38,46,47]. The HR-TEM image in Fig. 6b revealed that the  $\text{SnS}_2$

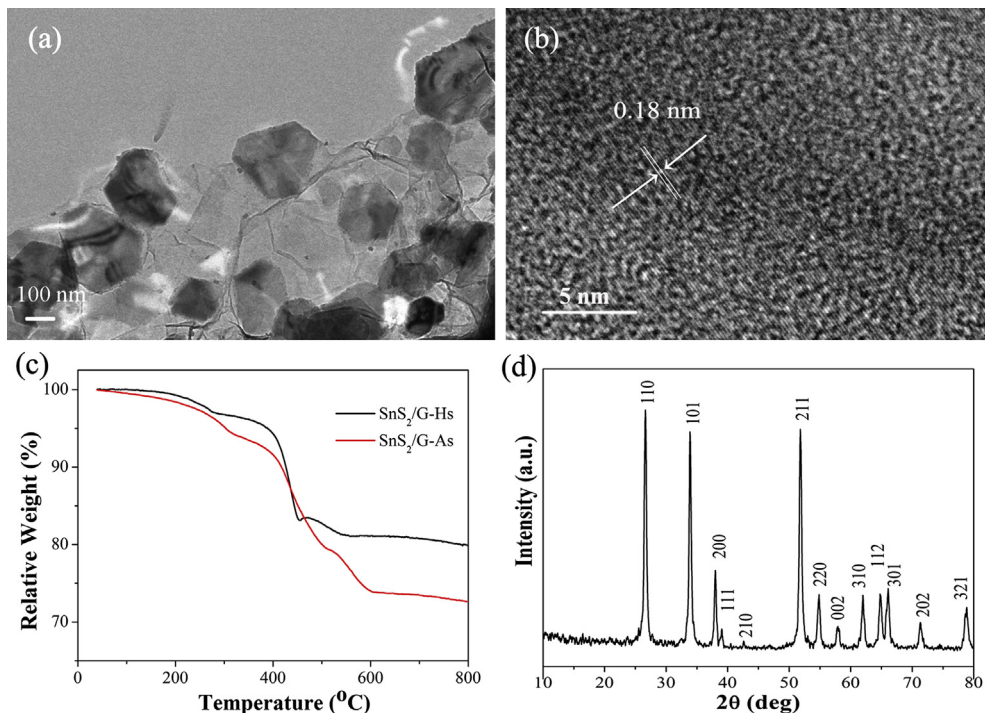


**Fig. 6.** TEM (a) and HRTEM (b) images of  $\text{SnS}_2/\text{G-As}$ . TG profiles of  $\text{SnS}_2/\text{G-Hs}$  and  $\text{SnS}_2/\text{G-As}$  (c). The wide-angle XRD pattern of the residue of  $\text{SnS}_2/\text{G-As}$  obtained after thermogravimetric analysis (d).

nanoplates were single crystalline with interplanar spacing of 0.18 nm, which could be assigned to the (110) crystalline plane. The thermal stability of SnS<sub>2</sub>/G-Hs and SnS<sub>2</sub>/G-As had been studied by thermogravimetric analysis (TGA) measurements, as shown in Fig. 6c. Both of two kinds of composites showed similar regions of weight loss on increasing the temperature. The initial weight loss from room temperature to 300 °C was due to the removal of absorbed water and the decomposition of residual oxygen groups in the graphene [48]. The second weight loss between 300 °C and 450 °C could be ascribed to the phase transformation from SnS<sub>2</sub> to SnO<sub>2</sub> [49–51]. The last weight loss step between 450 °C and 600 °C was assigned to the decomposition of graphene and oxidation of SnS<sub>2</sub> into SnO<sub>2</sub> [42]. As displayed in Fig. 6d, the residue of SnS<sub>2</sub>/G-As obtained after thermogravimetric analysis shown clear diffraction lines corresponding to tetragonal crystalline structure of SnO<sub>2</sub> [JCPDS 77–0452]. The weight fraction of graphene in SnS<sub>2</sub>/G-Hs and SnS<sub>2</sub>/G-As were ca. 3.9% and ca. 14.3%, respectively. As mentioned above, the concentration of graphene sheets was a crucial property for constructing the 3D assembly. The as-prepared GO sheets were reduced to graphene by H<sub>2</sub>S in situ released from NH<sub>2</sub>CSNH<sub>2</sub> during the hydrothermal process, and the reduced GO sheets could be easily restacked into a 3D architecture driven by combined hydrophobic and π–π stacking interactions, due to the decrease of oxygenated groups on the graphene sheets. On the other hand, Sn<sup>4+</sup> anchoring onto the GO sheet could also act as active sites for assembly with another GO sheet and SnS<sub>2</sub> facilitated stabilizing such novel graphene hydrogels [29,31,52–54]. Meanwhile, SnS<sub>2</sub> nanoplates as the support could effectively prevent the tight restacking of the graphene sheets to form a loose structure with rough surface, which increased the interfacial areas between electrolyte/electrode and thus improved lithium ions diffusion and electron transport.

Electrochemical properties of as-synthesized samples were investigated using a two-electrode cell with lithium metal as the counter electrode. Cycle voltammetry (CV) of SnS<sub>2</sub> NPs and SnS<sub>2</sub>/G-As for the first four cycles were evaluated in the 0.01–3.00 V voltage range at 0.5 mV s<sup>-1</sup> (Fig. 7a and b). For the SnS<sub>2</sub>/G-As composites, as shown in Fig. 7b, the peaks at 0.58, 1.13 and 1.53 V in the first cathodic sweep corresponded to the decomposition of the SnS<sub>2</sub> into metallic tin and the formation of Li<sub>2</sub>S (Eq. (2)), that may occurred in three steps as suggested by Kim et al. [55], as well as the formation of solid electrolyte interface (SEI) [56]. The peak at 0.30 V in the first cathodic scan represented the reversible formation Li<sup>x</sup>Sn alloy and the Li intercalation in GNS (Eqs. (1) and (3)). The additional peak at 1.76 V in the first cathodic scan, which was not yet observed during the subsequent cycles, could be attributed to the lithium intercalation of the SnS<sub>2</sub> layers without phase decomposition. The oxidation peak at 0.62 V in the first anodic scan were known to represent the delithiation reaction of Li<sup>x</sup>Sn alloy (Eq. (3)), while another oxidation peak at 1.92 V possibly originated from the oxygenation of Sn nanoparticles at higher potential in the charged state [57]. Those peaks were also generally consistent with that of the SnS<sub>2</sub>/G-Hs, indicating similar electrochemical reaction pathway of the two electrode materials (Fig. S2a). The CV curves of SnS<sub>2</sub> NPs were displayed in Fig. 7a, which were different from those of SnS<sub>2</sub>/G-As. The cathodic peak at 0.30 V could be totally attributed to the reaction of Li ions subsequently reacted with Sn metal to form Li<sup>x</sup>Sn alloy, while all of those peak currents decreased gradually from the second cycle. No peak at about 1.70 V in the first cathodic scan was seen, which might be assigned to the aggregation of pure SnS<sub>2</sub> nanoplates [58]. Two oxidation peaks at 0.67 and 1.68 V in the first anodic scan corresponded to delithiation reaction of Li<sup>x</sup>Sn alloy and the oxygenation of Sn nanoparticles, respectively. Fig. 7c and d shows the galvanostatic charge and discharge profiles (1st, 5th, 10th, 20th, 30th cycles) of SnS<sub>2</sub> NPs and SnS<sub>2</sub>/G-As in the range of

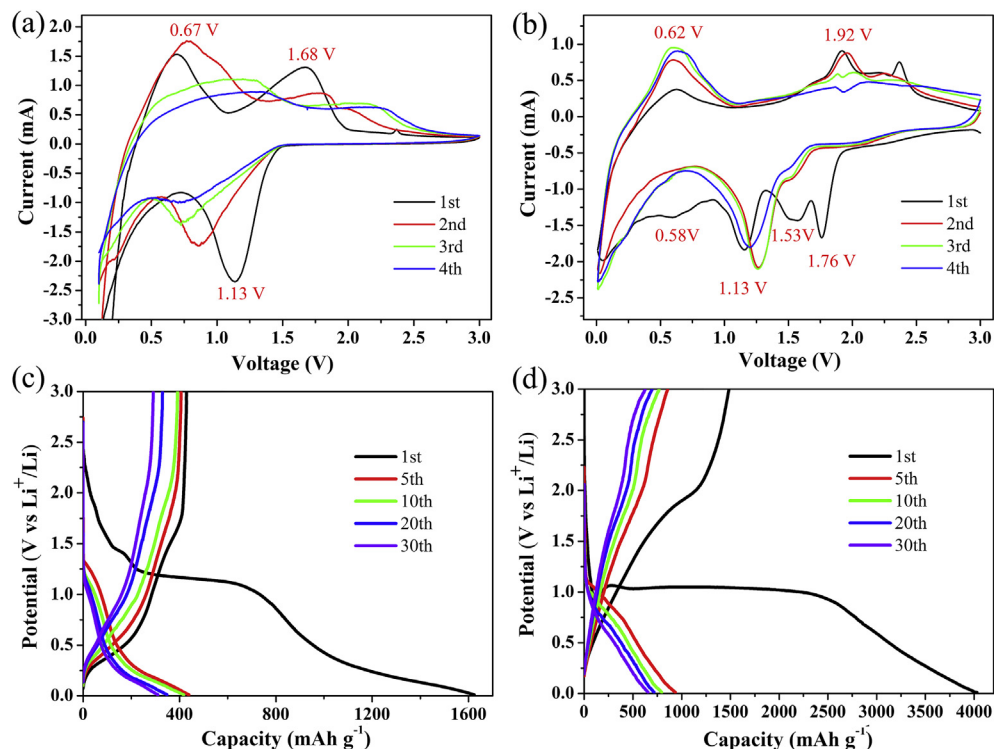
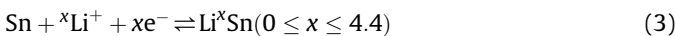


**Fig. 7.** Cyclic voltammograms of SnS<sub>2</sub> NPs (a) and SnS<sub>2</sub>/G-As (b) electrode between 0.01 and 3.00 V at a scan rate of 0.5 mV s<sup>-1</sup> for the first four cycles. Charge/discharge profiles of SnS<sub>2</sub> NPs (c) and SnS<sub>2</sub>/G-As (d) at a current density of 50 mA g<sup>-1</sup> in a voltage window of 0.01–3.00 V: the discharge curves in the 1st, 5th, 10th, 20th and 30th cycles.

0.01–3.00 V vs. Li/Li<sup>+</sup> at a current density of 50 mA g<sup>-1</sup>, respectively. All the charge/discharge shown plateaus consistent with the peaks in the CV curves, which were also well documented in the literature [7,12,55,56]. The SnS<sub>2</sub>/G-As electrode exhibited a very high first discharge (lithium insertion) capacity of 4030 mA h g<sup>-1</sup>. This was attributed to super-large specific surface area and large numbers of macropores in the unique 3D network structures of aerogel, which led to store more lithium ions, and electrolyte decomposition including that the lithium salt (LiPF<sub>6</sub>) decomposed thermally to LiF and PF<sub>5</sub> and solvent molecules were mainly reduced to ROCO<sub>2</sub>Li and ROLi compounds at the electrode surface [59]. The SnS<sub>2</sub>/G-As electrode was able to deliver a subsequent charge capacity of 1485 mA h g<sup>-1</sup> when charged to 3.00 V (lithium extraction), leading to an initial coulombic efficiency of 37% (Fig. 7d). The initial discharge and charge capacity were 1623 mA h g<sup>-1</sup> and 430 mA h g<sup>-1</sup> with a coulombic efficiency of 26% for the SnS<sub>2</sub> NPs electrode (Fig. 7c), and 2975 mA h g<sup>-1</sup> and 1102 mA h g<sup>-1</sup> with a coulombic efficiency of 37% for the SnS<sub>2</sub>/G-Hs electrode (Fig. S2b). This initial capacity loss could be possibly attributed to the formation of a solid electrolyte interface (SEI) layer on the electrode surface and the irreversible reaction (Eq. (2)), besides, the irreversible insertion of the Li ion in the graphene of SnS<sub>2</sub>/G-Hs and SnS<sub>2</sub>/G-As materials [42]. The discharge and charge capacities of SnS<sub>2</sub>/G-As electrode in the 5th cycle were 936 and 857 mA h g<sup>-1</sup>, respectively, giving rise to a coulombic efficiency of 92%. The shape of the profiles did not change significantly during the following cycling, indicating the stability of the electrode materials.



The cycling performances of SnS<sub>2</sub> NPs (A), SnS<sub>2</sub>/G-Hs (B) and SnS<sub>2</sub>/G-As (C) were evaluated in a potential range of 0.01–3.00 V (vs. Li<sup>+</sup>/Li) at a constant current rate of 50 mA g<sup>-1</sup>, and the results were displayed in Fig. 8a. SnS<sub>2</sub>/G-As manifested extraordinary cycling behavior and still retained a high reversible capacity of 656 mA h g<sup>-1</sup> after 30 cycles, which was higher than its theoretical capacity (630 mA h g<sup>-1</sup>). According to the compositions of the aerogel, and the specific capacity of SnS<sub>2</sub> (645 mA h g<sup>-1</sup>) and graphene (540 mA h g<sup>-1</sup>) [21], its theoretical capacity was calculated in the following section.

$$C_{\text{Theoretical}} = C_{\text{SnS}_2} \times \% \text{mass of SnS}_2 + C_{\text{graphene}} \times \% \text{mass of graphene}$$

$$= (645 \times 0.86 + 540 \times 0.14) = 630 \text{ mA h g}^{-1}$$
(4)

The corresponding coulombic efficiency increased from 37% in the first cycle to over 95% in the subsequent cycles (Fig. S3). On the contrary, for pure SnS<sub>2</sub> NPs and SnS<sub>2</sub>/G-Hs, a much lower capacity of 310 mA h g<sup>-1</sup> and 514 mA h g<sup>-1</sup> were delivered respectively, with the same coulombic efficiency of about 94% after 30 cycles. The observation above demonstrated that the incorporation of graphene not only significantly enhanced the specific capacities of the composites but also improved their cycling stabilities. Furthermore, the graphene sheets in the SnS<sub>2</sub>/G-As were seamlessly interconnected into a 3D interconnected networks, giving the material large surface area with macroporous structures, which encouraged more Li lithium ions storage and facilitated electrolyte contact as well as ionic diffusion, as well as outstanding electrical conductivity that was superior to that of SnS<sub>2</sub>/G-Hs. Thereby SnS<sub>2</sub>/G-As

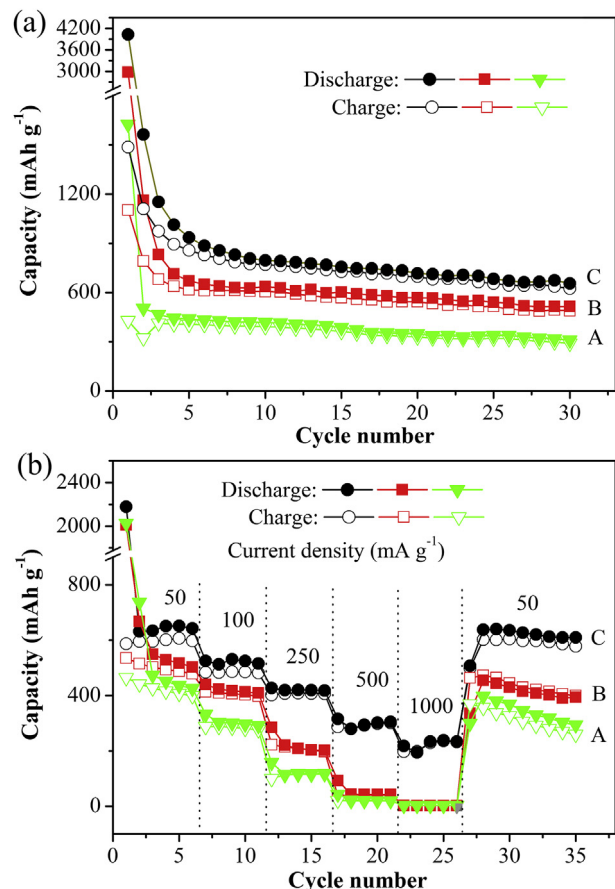


**Fig. 8.** Charge–discharge cycling performances of SnS<sub>2</sub> NPs (A), SnS<sub>2</sub>/G-Hs (B) and SnS<sub>2</sub>/G-As (C) electrodes at a current density of 50 mA g<sup>-1</sup> (a). Rate cycling performances of SnS<sub>2</sub> NPs (A), SnS<sub>2</sub>/G-Hs (B) And SnS<sub>2</sub>/G-As (C) electrodes at various current densities (b). All charge–discharge measurements were conducted between 0.01 and 3.00 V.

electrode exhibited an improved capacity and favorable cycling performance, compared to SnS<sub>2</sub>/G-Hs electrode.

More exciting results came from the rate performance of SnS<sub>2</sub>/G-As. Fig. 8b shown the rate cycling performances of the three samples at various rates between 50 and 1000 mA g<sup>-1</sup>. The reversible capacity of SnS<sub>2</sub>/G-As was stable at about 642 mA h g<sup>-1</sup> after 6 cycles at a rate of 50 mA g<sup>-1</sup>. Upon increasing the discharge–charge rates to 100, 250 and 500 mA g<sup>-1</sup>, the reversible capacities were maintained at about 525, 419 and 300 mA h g<sup>-1</sup>, respectively. It was obviously that all the rate capacities of SnS<sub>2</sub>/G-As were higher than those of pure SnS<sub>2</sub> NPs and SnS<sub>2</sub>/G-Hs. Even at a high current density of 1000 mA g<sup>-1</sup>, the specific capacity remained at about 240 mA h g<sup>-1</sup>, whereas that of SnS<sub>2</sub> NPs and SnS<sub>2</sub>/G-Hs dropped to only 1.9 mA h g<sup>-1</sup>. Actually, the 3D macroporous structures within SnS<sub>2</sub>/G-As had important influence on enhancing the charge/discharge rate performance, since the macroporous networks made it easier for the lithium ions to reach the active sites and minimized transport distances between electrode and electrolyte. When the current rate was again reduced back to 100 mA g<sup>-1</sup> after more than 26 cycles, the specific capacities of SnS<sub>2</sub>/G-As returned to the last values, which did not ultimately change in the subsequent cycles, indicating extraordinarily high cycling stabilities. Hence, SnS<sub>2</sub>/G-As electrode appeared to be useful for situations where quick charge and discharge were desired.

The high capacity, cycling stability and rate capability of the SnS<sub>2</sub>/G-As composites could be attributed to the unique structural feature of the aerogels and the synergistic effects of the layered

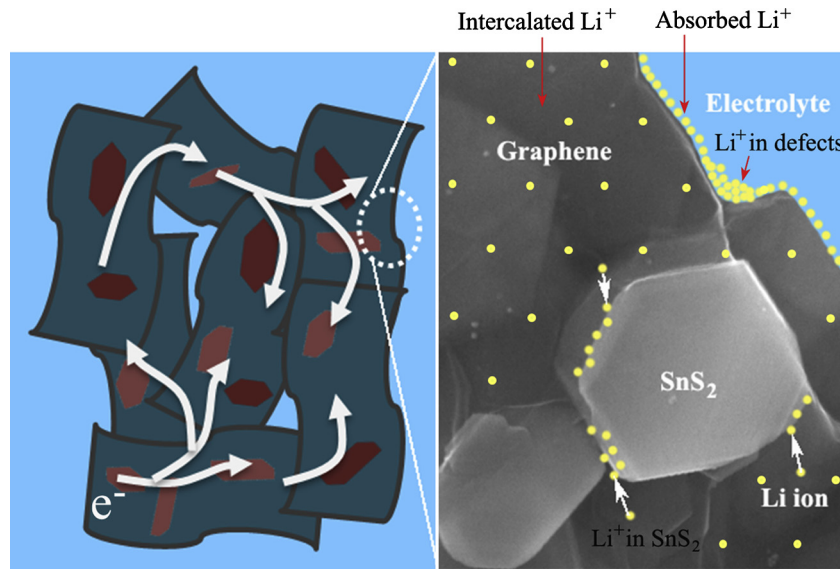


**Fig. 9.** Schematic representation of electron transmission and lithium ions storage in SnS<sub>2</sub>/G-As.

SnS<sub>2</sub> and the graphene. Firstly, as illustrated in Fig. 9, the interconnected graphene networks could serve as channels for enabling fast electron transport along all 3D direction. Secondly, the large surface area and large numbers of mesopores and macropores in SnS<sub>2</sub>/G-As lead to sufficient electrode/electrolyte interface, thus providing rich sites for absorbing lithium ions and minimizing transport distance between electrode and electrolyte. And the 3D macroporous structures allowed for effective ion migration into the active sites, thereby generating reversible capacitive behavior even at high charging/discharging rates. Finally, graphene sheets could inhibit the aggregation of SnS<sub>2</sub> nanoplates and act as buffers to accommodate the volume expansion/contraction of SnS<sub>2</sub> during Li<sup>+</sup> insertion/extraction process, resulting in good cyclic stability. The above advantages combined with the synergistic effect between the layered SnS<sub>2</sub> and the graphene together made SnS<sub>2</sub>/G-As achieve excellent electrochemical performance as promising anode materials for high-performance LIBs.

#### 4. Conclusions

In conclusion, 3D SnS<sub>2</sub>/graphene aerogels have been successfully fabricated via a facile in situ hydrothermal method for self-assembly of graphene sheets which embedded SnS<sub>2</sub> nanoplates, then freeze-drying to maintain the 3D monolithic architectures. The obtained aerogels with interconnected networks provided high surface area, 3D macroporosity and high electrical conductivity, as well as enhancing the synergistic interactions between the layered SnS<sub>2</sub> and the graphene by increasing their contact areas. As a result, SnS<sub>2</sub>/G-As shown high reversible capacity (656 mA h g<sup>-1</sup>) and excellent rate capability (240 mA h g<sup>-1</sup> at the rate of 1000 mA g<sup>-1</sup>) when used as an anode in rechargeable LIBs, which were higher than pure SnS<sub>2</sub> NPs and SnS<sub>2</sub>/G-Hs. Furthermore, the self-assembly of the 3D macrostructure could provide a convenient, efficient and low-cost method to fabricate other 3D graphene-based hybrid materials for wide applications in areas such as supercapacitors, catalysis, and photovoltaic devices.

#### Acknowledgments

We thank the National Natural Science Foundation of China (21236003, 21206042, 20925621, 20976054, and 21176083), the

Special Projects for Nanotechnology of Shanghai (11nm0500800) the Fundamental Research Funds for the Central Universities (WD1013015 and WD1114005), and the Program for Changjiang Scholars and Innovative Research Team in University (IRT0825), and the Shanghai Leading Academic Discipline Project (project number: B502) for financial supports.

#### Appendix A. Supplementary data

Supplementary data related to this article can be found at <http://dx.doi.org/10.1016/j.jpowsour.2013.03.048>.

#### References

- [1] M. Winter, J.O. Besenhard, M.E. Spahr, P. Novák, *Adv. Mater.* 10 (1998) 725–763.
- [2] C. Liu, F. Li, L.P. Ma, H.M. Cheng, *Adv. Mater.* 22 (2010) 28–62.
- [3] M. Winter, R.J. Brodd, *Chem. Rev.* 104 (2004) 4245–4270.
- [4] F.M. Courtel, E.A. Baranova, Y. Abu-lebuddh, I.J. Davidson, *J. Power Sources* 195 (2010) 2355–2361.
- [5] Z.Y. Wang, Y. Li, J.Y. Lee, *Electrochim. Commun.* 11 (2009) 1179–1182.
- [6] G. Du, Z.P. Guo, S. Wang, R. Zeng, Z. Chen, H. Liu, *Chem. Commun.* 46 (2010) 1106–1108.
- [7] J.W. Seo, J.T. Jang, S.W. Park, C. Kim, B. Park, J. Cheon, *Adv. Mater.* 20 (2008) 4269–4273.
- [8] J.W. Seo, Y.W. Jun, S.W. Park, H. Nah, T. Moon, B. Park, J.G. Kim, Y.J. Kim, J. Cheon, *Angew. Chem. Int. Ed.* 46 (2007) 8828–8831.
- [9] Y. Idota, T. Kubota, A. Matsufuji, Y. Maekawa, T. Miyasaka, *Science* 276 (1997) 1395–1397.
- [10] I.A. Courtney, J.R. Dahn, *J. Electrochem. Soc.* 144 (1997) 2943–2948.
- [11] J.M. Ma, D.N. Lei, L. Mei, X.C. Duan, Q.H. Li, T.H. Wang, W.J. Zheng, *CrysEngComm* 14 (2012) 832–836.
- [12] C.X. Zhai, N. Du, H.Z.D. Yang, *Chem. Commun.* 47 (2011) 1270–1272.
- [13] J.T. Zai, K.X. Wang, Y.Z. Su, X.F. Qian, J.S. Chen, *J. Power Sources* 196 (2011) 3650–3654.
- [14] N. Du, H. Zhang, J. Liu, L.T. Chang, L. Wang, J.Z. Jiang, *Nanoscale* 4 (2012) 4002–4006.
- [15] S. Liu, X.M. Yin, L.B. Chen, Q.H. Li, T.H. Wang, *Solid State Sci.* 12 (2010) 712–718.
- [16] Z.F. Jiang, C. Wang, G.H. Du, Y.J. Zhong, J.Z. Jiang, *J. Mater. Chem.* 22 (2012) 9494–9496.
- [17] B. Luo, Y. Fang, B. Wang, J.S. Zhou, H.H. Song, L.J. Zhi, *Energy Environ. Sci.* 5 (2012) 5226–5230.
- [18] M. Pumera, *Chem. Rec.* 9 (2009) 211–223.
- [19] M. Pumera, *Energy Environ. Sci.* 4 (2011) 668–674.
- [20] R.R. Nair, P. Blake, A.N. Grigorenko, K.S. Novoselov, T.J. Booth, T. Stauber, N.M.R. Peres, A.K. Geim, *Science* 320 (2008) 1308.
- [21] E.J. Yoo, J. Kim, E. Hosono, H.S. Zhou, T. Kudo, I. Honma, *Nano Lett.* 8 (2008) 2277–2282.

- [22] C. Uthaisar, V. Barone, *Nano Lett.* 10 (2010) 2838–2842.
- [23] N. Lavoie, P.R.L. Malenfant, F.M. Courtel, Y. Abu-Lebdeh, I.J. Davidson, *J. Power Sources* 213 (2012) 249–254.
- [24] Z.S. Wu, W.C. Ren, L. Wen, L.B. Gao, J.P. Zhao, Z.P. Chen, G.M. Zhou, F. Li, H.M. Cheng, *ACS Nano* 4 (2010) 3187–3194.
- [25] X.L. Yang, K.C. Fan, Y.H. Zhu, J.H. Shen, X. Jiang, P. Zhao, C.Z. Li, *J. Mater. Chem.* 22 (2012) 17278–17283.
- [26] S.M. Paek, E. Yoo, I. Honma, *Nano Lett.* 9 (2009) 72–75.
- [27] D.H. Wang, R. Kou, D. Choi, Z.G. Yang, Z.M. Nie, J. Li, L.V. Saraf, D.H. Hu, J.G. Zhang, G.L. Graff, J. Liu, M.A. Pope, I.A. Aksay, *ACS Nano* 4 (2010) 1587–1595.
- [28] S.B. Yang, X.L. Feng, K. Müllen, *Adv. Mater.* 23 (2011) 3575–3579.
- [29] Y.X. Xu, K.X. Sheng, C. Li, G.Q. Shi, *ACS Nano* 4 (2010) 4324–4330.
- [30] J. Chen, K.X. Sheng, P.H. Luo, C. Li, G.Q. Shi, *Adv. Mater.* 24 (2012) 4569–4573.
- [31] Z.H. Tang, S.L. Shen, J. Zhuang, X. Wang, *Angew. Chem. Int. Ed.* 49 (2010) 4603–4607.
- [32] H.C. Bi, X. Xie, K.B. Yin, Y.L. Zhou, S. Wan, L.B. He, F. Xu, F. Banhart, L.T. Sun, R.S. Ruoff, *Adv. Funct. Mater.* (2012), <http://dx.doi.org/10.1002/adfm.201200888>.
- [33] Z.S. Wu, S.B. Yang, Y. Sun, K. Parvez, X.L. Feng, K. Müllen, *J. Am. Chem. Soc.* 134 (2012) 9082–9085.
- [34] C.G. Hu, H.H. Cheng, Y. Zhao, Y. Hu, Y. Liu, L.M. Dai, L.T. Qu, *Adv. Mater.* 24 (2012) 5493–5498.
- [35] N.I. Kovtyukhova, P.J. Ollivier, B.R. Martin, T.E. Mallouk, S.A. Chizhik, E.V. Buzaneva, A.D. Gorchinskii, *Chem. Mater.* 11 (1999) 771–778.
- [36] J.H. Shen, Y.H. Zhu, K.F. Zhou, X.L. Yang, C.Z. Li, *J. Mater. Chem.* 22 (2012) 545–550.
- [37] K. Chang, W.X. Chen, *ACS Nano* 5 (2011) 4720–4728.
- [38] K. Chang, Z. Wang, G.C. Huang, H. Li, W.X. Chen, J.Y. Lee, *J. Power Sources* 201 (2011) 259–266.
- [39] G. Lucovsky, J.C. Mikkelsen Jr., *Phys. Rev. B Solid State* 14 (1976) 1663–1669.
- [40] D. Graf, F. Molitor, K. Ensslin, C. Stampfer, A. Jungen, C. Hierold, L. Wirtz, *Nano Lett.* 7 (2007) 238–242.
- [41] O. Akhavan, *ACS Nano* 4 (2010) 4174–4180.
- [42] M. Sathish, S. Mitani, T. Tomai, I. Honma, *J. Phys. Chem. C* 116 (2012) 12475–12481.
- [43] Z.Y. Zhang, C.L. Shao, X.H. Li, Y.Y. Sun, M.Y. Zhang, J.B. Mu, P. Zhang, Z.C. Guo, Y.C. Liu, *Nanoscale* 5 (2013) 606–618.
- [44] Y.C. Zhang, Z.N. Du, S.Y. Li, M. Zhang, *Appl. Catal. B* 95 (2010) 153–159.
- [45] W.F. Chen, S.R. Li, C.H. Chen, L.F. Yan, *Adv. Mater.* 23 (2011) 5679–5683.
- [46] J.M. Ma, J. Zhang, S.R. Wang, Q.H. Wang, L.F. Jiao, J.Q. Yang, X.C. Duan, Z.F. Liu, J.B. Lian, W.J. Zheng, *CrystEngComm* 13 (2011) 6077–6081.
- [47] W.D. Shi, L.H. Huo, H.S. Wang, H.J. Zhang, J.H. Yang, P.H. Wei, *Nanotechnology* 17 (2006) 2918–2924.
- [48] W.F. Chen, L.F. Yan, P.R. Bangal, *Carbon* 48 (2010) 1146–1152.
- [49] M. Sathish, S. Mitani, T. Tomai, A. Unemoto, I. Honma, *J. Solid State Electrochem.* 16 (2012) 1767–1774.
- [50] C.X. Zhai, N. Du, H. Zhang, J.X. Yu, D. Yang, *ACS Appl. Mater. Interfaces* 3 (2011) 4067–4074.
- [51] J.R. Huang, K. Yu, C.P. Gu, M.H. Zhai, Y.J. Wu, M. Yang, J.H. Liu, *Sens. Actuators B* 147 (2010) 467–474.
- [52] X. Jiang, Y.W. Ma, J.J. Li, Q.L. Fan, W. Huang, *J. Phys. Chem. C* 114 (2010) 22462–22465.
- [53] S.J. Park, K.S. Lee, G. Bozoklu, W. Cai, S.T. Nguyen, R.S. Ruoff, *ACS Nano* 2 (2008) 572–578.
- [54] H.P. Cong, X.C. Ren, P. Wang, S.H. Yu, *ACS Nano* 6 (2012) 2693–2703.
- [55] T.J. Kim, C. Kim, D. Son, M. Choi, B. Park, *J. Power Sources* 167 (2007) 529–535.
- [56] T. Momma, N. Shiraishi, A. Yoshizawa, T. Osaka, A. Gedanken, J. Zhu, L. Sominshi, *J. Power Sources* 87 (2001) 198–200.
- [57] Y.P. Du, Z.Y. Yin, X.H. Rui, Z.Y. Zeng, X.J. Wu, J.Q. Liu, Y.Y. Zhu, J.X. Zhu, X. Huang, Q.Y. Yan, H. Zhang, *Nanoscale* 5 (2013) 1456–1459.
- [58] C.F. Shen, L.Y. Ma, M.B. Zheng, B. Zhao, D.F. Qiu, L.J. Pan, J.M. Cao, Y. Shi, J. Solid State Electrochem. 16 (2012) 1999–2004.
- [59] V. Etacheri, R. Marom, R. Elazari, G. Salitra, D. Aurbach, *Energy Environ. Sci.* 4 (2011) 3243–3262.